Film Morphology of High Efficiency Solution-Processed Small-Molecule Solar Cells

John A. Love, Christopher M. Proctor, Jianhua Liu, Christopher J. Takacs, Alexander Sharenko, Thomas S. van der Poll, Alan J. Heeger, Guillermo C. Bazan, and Thuc-Quyen Nguyen**

Morphological control over the bulk heterojunction (BHJ) microstructure of a high-efficiency small molecule photovoltaic system is demonstrated using both thermal treatment and solvent additive processing. Single crystal X-ray diffraction is utilized to understand molecular interactions in the solid state and the BHJ morphology is examined using bright field, high-resolution, and cross-section transmission electron microscopy techniques. Controlling the domain size, while maintaining good molecular order within the semiconducting donor material, is found to be crucial in achieving high performance and over 90% internal quantum efficiency exhibited under the optimized conditions.

1. Introduction

Solution-deposited organic solar cells are of keen interest as they have the potential to be fabricated via high throughput methods such as roll-to-roll coating and ink-jet printing.[1–3] Optimization of their active layers requires convergence of a range of materials science and engineering expertise, including organic chemistry, emerging nanoscale characterization methodologies, optical processes, and device physics. Two components, electron donor (D) and acceptor (A) materials, are cast simultaneously from solution and upon drying, yield a bulk heterojunction (BHJ) composite film. Several constraints must be managed within BHJ layers for efficient charge generation and extraction; these include the formation of interpenetrating networks of donor and acceptor phases such that photogenerated holes and electrons can be collected at the appropriate electrodes,[4] internal order within these phases, which can affect charge carrier transport,[5] and nanoscale phase separation so excitons can reach critical D/A interfaces.[6] In an ideal situation, all these morphological requirements are generated at the point of film formation. As such, BHJ structural control provides a significant challenge within the context of controlling self-assembly processes in soft matter.[7]

Examination of the literature shows that the vast majority of solution deposited BHJ devices and studies take advantage of blends containing conjugated polymers as the donor component and fullerene derivatives as the acceptor component.[8] However, devices with excellent power conversion efficiencies (PCEs) in which small molecules replace the conjugated polymer are beginning to emerge.[9–18] Part of the motivation behind using a small molecule system is their well-defined chemical structures, reduced batch-to-batch variability, and amenability to purification techniques commonly used for organic synthesis.[19,20]

Recently, we introduced the new molecular donor, 7,7′-(4,4-bis(2-ethylhexyl)-4H-silolo[3,2-b:4,5-b′]dithiophene-2,6-diyl)bis(6-fluoro-4-(5′-hexyl-[2,2′-bithiophen]-5-yl)benzo[*c*][1,2,5]thiadiazole), *p*-DTS(FBTTh$_2$)$_2$, to control chemical processes at interfaces.[13,21] As shown in **Figure 1** a, the carbon-fluorine bond in the electronic backbone provides an electron-withdrawing functionality without introducing basic heteroatoms,[22] rendering it inert towards the acidity of poly(3,4-ethylenedioxythiophene):poly(styrenesulfonicacid) (PEDOT:PSS). Furthermore, it was used in BHJ solar cells with phenyl-C71-butyric acid methyl ester, PC$_{71}$BM, producing one of the highest performance solution-processed molecular BHJ solar cells to date.

Achieving high PCE with *p*-DTS(FBTTh$_2$)$_2$ requires appropriate processing conditions. These effects are shown in Figure 1b; while a blend left as-cast from chlorobenzene gives a relatively modest PCE of 1.8%, thermal annealing leads to a simultaneous increase in open circuit voltage, (V_{OC}) fill factor, (*FF*) and short circuit current density, (J_{SC}) resulting in an overall increase in PCE up to 5.8%. If the active layer is instead cast from a solution containing a 0.4% diiodooctane (DIO) by volume as a high boiling point solvent additive,[23] the efficiency is further increased to 7.0%. The drastic changes in device performance associated with the different processing conditions are most likely due to variations in the resultant morphologies and therefore investigation of these different BHJ microstructures is critical for understanding the high PCE of this system. In this contribution, we specifically address the question of BHJ morphology in the high efficiency *p*-DTS(FBTTh$_2$)$_2$:PC$_{71}$BM organic solar cells described in Figure 1b and show that this

J. A. Love, C. M. Proctor, J. Liu, C. J. Takacs, A. Sharenko, T. S. van der Poll, A. J. Heeger, Prof. G. C. Bazan, Prof. T.-Q. Nguyen
Center for Polymers and Organic Solids
University of California
Santa Barbara, CA 93106, USA
E-mail: bazan@chem.ucsb.edu; quyen@chem.ucsb.edu

DOI: 10.1002/adfm.201300099

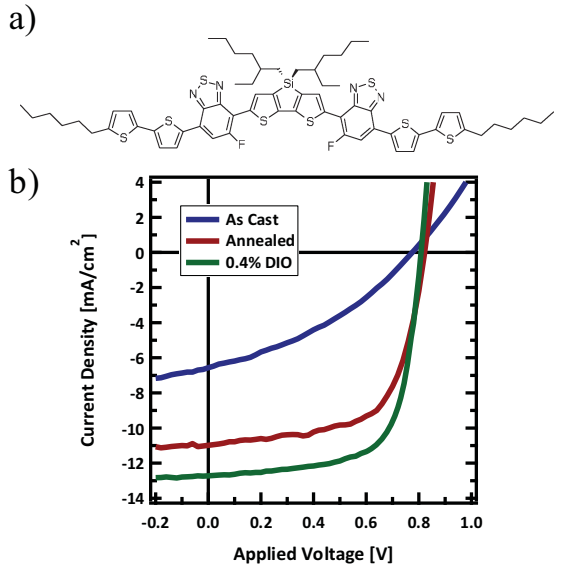

Figure 1. a) Molecular structure of *p*-DTS(FBTTh$_2$)$_2$. b) Solar cell performance of *p*-DTS(FBTTh$_2$)$_2$:PC$_{71}$BM system as a function of processing history, as-cast (blue), thermally annealed at 130 °C (red), and with 0.4% DIO additive (green).

donor molecule can achieve remarkable levels of organization within the active layer.

2. Results and Discussion

We wish to address both thermal annealing and addition of solvent additives on the morphological structure of *p*-DTS(FBTTh$_2$)$_2$:PC$_{71}$BM films, as each method leads to significant improvements in device efficiency. Morphological characterization was performed on films processed identically to those used for device fabrication, and while a general understanding of these processing techniques was desired, of particular interest were the optimum conditions, 130 °C for the case of thermal annealing and 0.4% DIO for the solvent additive process. As in device fabrication, the total concentration of the casting solution was held at 3.5 wt% and the *p*-DTS(FBTTh$_2$)$_2$:PC$_{71}$BM weight ratio kept at 3:2. The blend obtained by simply casting from chlorobenzene serves as the baseline system.

2.1. Morphological Characterization

2.1.1. UV-Visible Absorption

The influence of processing conditions on film properties was first examined through UV-visible absorption spectroscopy (**Figure 2**). The absorption of *p*-DTS(FBTTh$_2$)$_2$ in chloroform gives a maximum (λ_{max}) at 615 nm and an absorption onset (λ_{onset}) at 680 nm (Figure 2a). The value of λ_{onset} defines an optical bandgap of 1.8 eV. Thin films of neat *p*-DTS(FBTTh$_2$)$_2$ show a red-shift in absorption, with λ_{max} = 688 nm and λ_{onset} = 780 nm, corresponding to a 1.5 eV bandgap. The appearance of vibronic structure at 688 nm and the red-shift in λ_{onset} of 100 nm suggests good molecular ordering within the film.[24,25]

When *p*-DTS(FBTTh$_2$)$_2$ is cast from a blend with PC$_{71}$BM, (Figure 2b, black) λ_{max} (620 nm) is similar to what is observed in solution. This feature, in combination with the loss in vibronic structure, suggests that PC$_{71}$BM serves to break up some of the solid-state ordering seen in neat *p*-DTS(FBTTh$_2$)$_2$. As shown in Figure 2b, the vibronic structure reappears upon thermal annealing and becomes more pronounced with increasing temperature. We can surmise at this point that thermal annealing allows intermolecular motion within the film such that the molecular components can more readily achieve better organization.[26]

Films cast from solutions containing DIO exhibit similar phenomenology as those that undergo thermal treatment (Figure 2c). Just 0.25% additive by volume results in the reemergence of a vibronic peak at 670 nm, which, as described previously, is not evident in the blend cast from pure chlorobenzene. Subsequently, there is a clear, progressive increase in intensity of the vibronic peak and a red-shift of λ_{onset} as DIO increases up to 10%. Addition of large amounts of DIO yields slightly thinner films, so the spectra in Figure 1 are normalized to the peak at 625 nm to more clearly highlight the progression in vibronic structure.

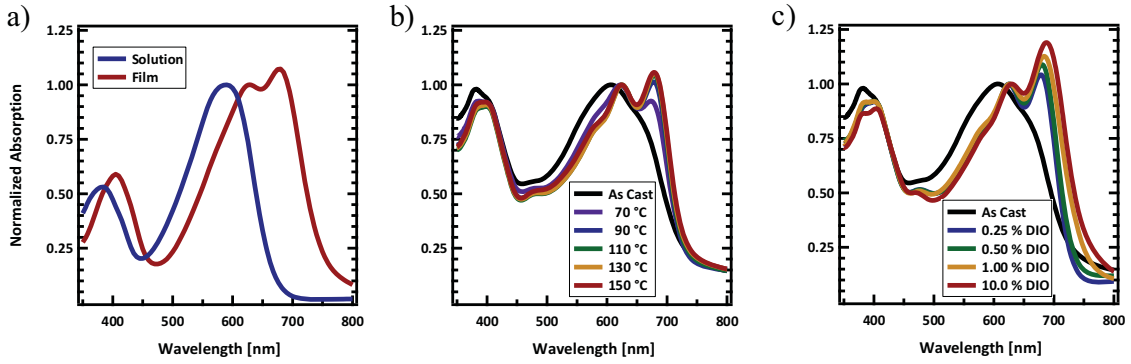

Figure 2. Normalized UV-visible absorption spectra of the a) neat *p*-DTS(FBTTh$_2$)$_2$ solution and film b) BHJ annealed films and c) BHJ films processed with DIO all cast on PEDOT:PSS coated ITO substrates.

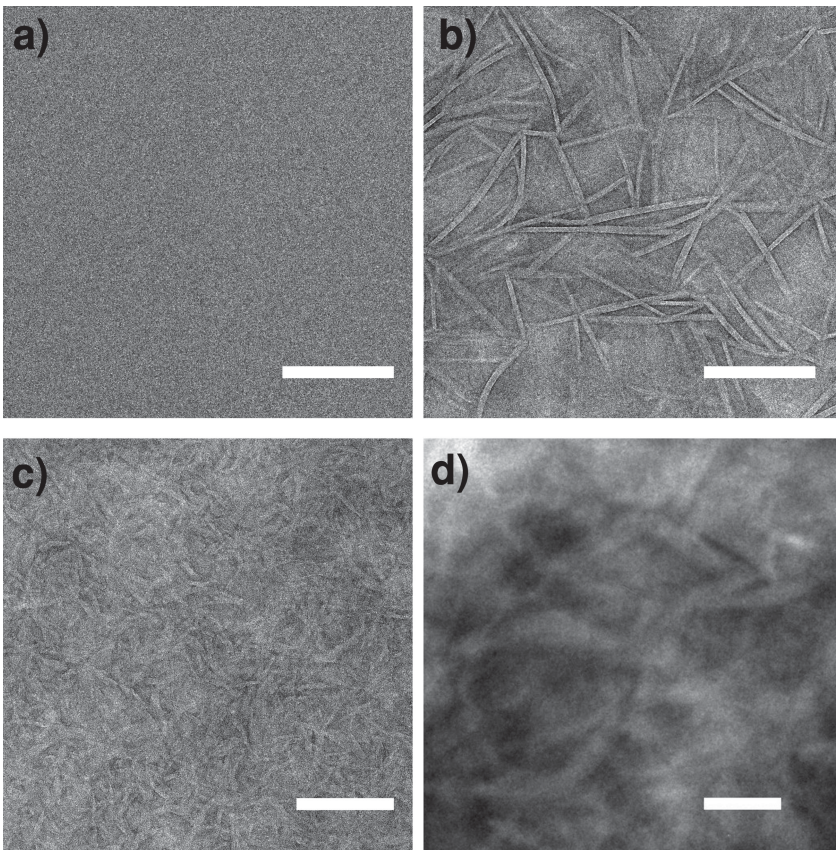

Figure 3. Bright field TEM images of *p*-DTS(FBTTh$_2$)$_2$:PC$_{71}$BM films a) as-cast from chlorobenzene, b) thermally annealed at 130 °C, c) cast from 0.4% DIO, and d) from 1.0% DIO. Scale bars all correspond to 200 nm.

2.1.2. Transmission Electron Microscopy

We employed transmission electron microscopy (TEM) to understand the origin of the observed changes in optical properties upon thermal treatment or use of solvent additive, and the nature of the molecular order suggested by the UV-visible spectra. Each BHJ film was imaged in bright field mode with a small amount of defocus (5–10 μm) and exposure times of 10–30 s to enhance the low contrast inherent to organic blends.[27] As seen in **Figure 3**a, the as-cast film shows almost no discernible structure, even at relatively large defocus values and various exposure conditions. Thus, when cast from chlorobenzene, *p*-DTS(FBTTh$_2$)$_2$ and PC$_{71}$BM seem to be well mixed, with no significant crystallization or phase separation observable. When these films are annealed, however, one observes wire-like structures that propagate throughout the film with characteristic widths of 40–50 nm and lengths of hundreds of nanometers. These domains are assigned as regions of *p*-DTS(FBTTh$_2$)$_2$ within the BHJ based on their high relative intensity (bright regions) compared to the surrounding film.[28] In addition, there appear to be larger scale phase fluctuations evidenced by the variations in contrast across the film, while any smaller scale structures that may exist between the wires lack significant contrast.

A different picture is observed in the film processed with 0.4% DIO. Smaller *p*-DTS(FBTTh$_2$)$_2$ domains are visible with good contrast compared to the surrounding. These grains have a characteristic size of about 30–40 nm and seem to form a continuous network throughout the film (Figure 3c). While the use of large values of defocus to induce contrast in organic films can introduce small-scale features into an image which do not correspond directly with microstructure,[29] the structures seen in Figure 3 remain apparent and unchanged across all levels of defocus (Figure S1, Supporting Information), helping to confirm the features are morphological, and not a consequence of imaging.

In films formed from 1% DIO solutions, conditions that lead to deterioration of PCE to less than 1% (Figure S2, Supporting Information), much larger scale wires are formed (Figure 3d). The wires have widths close to 100 nm and can be up to microns long (for a large-scale perspective of the wires, see Figure S3, Supporting Information). While 0.4% DIO helps induce a network of small grains of *p*-DTS(FBTTh$_2$)$_2$, too much DIO results in significantly larger *p*-DTS(FBTTh$_2$)$_2$ domains.

Further insight into the morphology can be gained through low-dose, high-resolution TEM. By adjusting the contrast transfer function through a small defocus (1–2 μm), it is possible to directly image crystal lattice fringes within the film.[30–32] This technique helps to understand the nature of crystallinity within the morphology seen using traditional bright field TEM. The crystals are highly sensitive to the electron beam, so care needs to be taken to minimize the dosage and avoid degradation. Images are obtained at a flux of 2.8 electrons Å^{-2} s and an exposure time of 4 s, approximately one third of the exposure time necessary for the fringes to disappear. A more detailed description of the image-taking process is described in the Experimental Section.

From **Figure 4**a, there is a clear correlation between the direction of the observed wires and the imaged lattice spacings

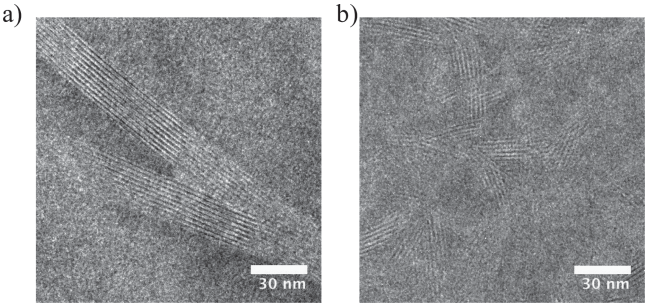

Figure 4. High-resolution TEM images of *p*-DTS(FBTTh$_2$)$_2$:PC$_{71}$BM films showing lattice fringes (0.3 Å^{-1}) from in-plane stacking of the *p*-DTS(FBTTh$_2$)$_2$ phase in a) thermally annealed, and b) 0.4% DIO processed BHJ films.

in the thermally annealed blend film. Fringes run along the length of the wires, corresponding to repeating 2.2 nm lattice planes across the width of the wires. It is also worth noting that additional lattice fringes with 1.6 nm spacing are visible in some of the images taken, in the areas between the wires (Figure S4, Supporting Information). This crystal population likely leads to some of the observed diffraction contrast in the high-resolution TEM images. However, these crystallites are particularly sensitive to electron beam damage, and disappear within a few hundred counts, making the extent of this crystal population difficult to quantify.

The structures in the optimum 0.4% DIO processed film (Figure 4b) are not nearly as well resolved or as coherent as in the annealed film. The same 2.2 nm spacing can be observed throughout the film, although the imaged crystalline domains are much smaller. The lattices form much shorter wires, making grain-like structures reminiscent of those seen by conventional TEM. This gives a good indication that the features seen in bright field TEM are due to crystalline *p*-DTS(FBTTh$_2$)$_2$.

One drawback of high-resolution TEM is that it is not sensitive to all orientations of crystals within the film; only lattices normal to the electron beam can be imaged.[27] The resultant image is a projection of the crystallites throughout the film which lie in-plane. Cross-sectional TEM was employed to examine the three dimensional nature of the BHJ morphology.[33–37] A focused ion beam (FIB) was used to mill out a TEM lamellar, and using an Omni probe system, attach it to a TEM grid. The sample was then further thinned to a thickness of approximately 75 nm in multiple etching steps working at a low voltage and using progressively lower operating currents. Particular care was taken to not expose the sample to any unnecessary dose of either the ion or electron beams to reduce the amount of FIB damage and implantation as much as possible, as these can cause difficulty in the interpretation of cross-sectional samples.[38]

Rather than looking at the as-cast, annealed, and solvent additive conditions separately, all three BHJ films were deposited on top of each other in a stacked manner. The utility of such a stacked configuration, beyond allowing the simultaneous preparation and imaging of all three systems of interest at once, is reduction in the ambiguity that might result from thickness variations, ion beam damage, or gallium implantation.[36] Any artifacts visible in one layer should also be present and equal in each of the other layers. In order to fabricate such samples, films were prepared successively with thin titanium oxide layer spacers.[37] Before casting the successive BHJ layers, relatively thick layers of PEDOT:PSS were applied to each titanium oxide layer to create a nearly equivalent architecture to that found in working devices. Detailed information on the preparation of these stacks can be found in the Experimental Section. It bears noting that the order in which the BHJ films are deposited was chosen due to the thermal requirements of each film, as any annealing steps affect all of the deposited layers. Thus, the first layer was annealed prior to subsequent layer depositions.

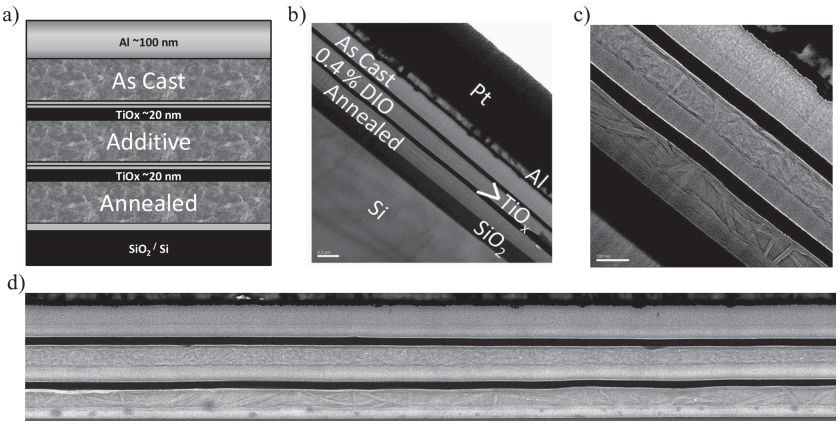

Figure 5. a) Cartoon schematic of multilayer stack, b) cross-sectional TEM of multilayer stack at 7 µm defocus showing stack architecture, c) small section of a stack at 7 µm defocus, and d) multilayer sample from stitched images at 5 µm defocus.

The results from the cross-sectional TEM studies are shown in **Figure 5**. Differences between the three film structures can be easily observed. The wire-type structures seen in the top-down images of the annealed film, that is, Figures 3b,4a, are also present in the cross-section. These wires do not seem to have a preferential orientation, but rather propagate throughout the film oscillating vertically. We also bring attention to what seems to be a coating of *p*-DTS(FBTTh$_2$)$_2$ directly atop the PEDOT:PSS layer in the annealed film, that covers the entire width of the slice. While we cannot draw conclusions about the extent of this layer from such a small fraction of the film, it was seen independently in two different FIB cross sectional images.

Although the network within the *p*-DTS(FBTTh$_2$)$_2$:PC$_{71}$BM film processed with 0.4% DIO is not as easy to discern as the wire structures in the thermally annealed film, it again correlates well with the top-down images in Figures 3c,4b. This particular *p*-DTS(FBTTh$_2$)$_2$:PC$_{71}$BM blend exhibits finer-scale phase separation than in the annealed film. The "rice-grain" structure seen in-plane in the top down TEM seems to extend vertically as well. The lack of discernible structure within the as-cast layer of the stack is further evidence that the materials are well blended when cast from chlorobenzene alone.

2.1.3. Single Crystal Structure

One of the promising features of discrete molecular systems, such as *p*-DTS(FBTTh$_2$)$_2$, compared to conjugated polymer counterparts is the possibility to obtain a complete picture of the distance and orientation between the optoelectronic units in the solid state via single crystal X-ray diffraction studies. Indeed, it was possible to grow suitable single crystals of *p*-DTS(FBTTh$_2$)$_2$ from a chloroform solution through vapor diffusion of hexane. The resulting crystal possesses a triclinic system with two molecules assigned to a unit cell, as shown in **Figure 6**. The conjugated backbone remains planar, with almost no twisting. Such a flat conformation enables intramolecular interaction between the electron-poor fluorinated benzothiadiazole (FBT) moieties

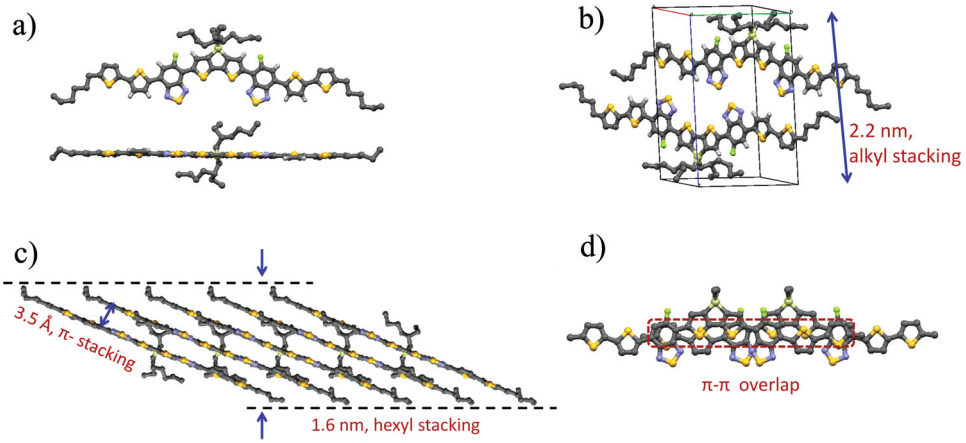

Figure 6. a) Molecular conformation of *p*-DTS(FBTTh$_2$)$_2$ with C, N, S and F atoms shown in grey, blue, yellow, and green respectively. b) Unit cell showing 2.2 nm alkyl spacing c) viewed down (1,4,1) plane highlighting π-stacking and hexyl stacking. d) Intermolecular π-conjugated backbone overlap of adjacent molecules viewed perpendicular to the plane of the conjugated backbone. Alkyl chains (2-ethylhexyl) are simplified as methyl groups for clarity.

and the electron-rich silyldithiophene (SDT) and bithiophene moieties, and extends the molecule's conjugation length. Besides the intramolecular conformation, *p*-DTS(FBTTh$_2$)$_2$ packs in a slip-stack fashion (Figure 6c) forming a two-dimensional columnar array, which is favorable for intermolecular charge transport,[39,40] as opposed to the "herringbone" packing commonly observed in many conjugated small molecules such as oligothiophenes,[41–43] and diketopyrrolopyrrole derivatives.[44,45]

Intermolecular overlap of conjugated backbones geometrically provides the capacity for π-orbital interaction, critical for charge carrier hopping during transport.[46] Many conjugated molecules only show overlap at their end-groups or the edge of the conjugated backbone, leading to a small area with direct π–π overlap. A superior π–π overlapping area is observed between two adjacent *p*-DTS(FBTTh$_2$)$_2$ molecules as shown in Figure 6d (as highlighted by the red rectangle) in which nearly the entire conjugated backbone, including the DTS core, FBT units and two of the four thienyl units, have direct overlap with neighboring molecules. This overlap, intrinsic to the solid state arrangement of *p*-DTS(FBTTh$_2$)$_2$, may have merit for effective charge transport.

Since single crystal growth is an inherently different process than casting a thin film, grazing incidence wide-angle X-ray scattering was used to probe the crystallites within the thin film (Figure S5, Supporting Information). The diffraction pattern was indexed according to the obtained crystal structure and the good correlation supports that the single crystal and crystallites within the spin coated thin film are of the same polymorph. The π-stacking within the crystal has a distance of 3.5 Å between two adjacent conjugated backbones that can be described by the (141) plane. There is an orthogonal spacing at 2.2 nm in the (001) direction, which describes the "alkyl stacking" corresponding to the ethyl hexyl side chains of the dithienosilole unit spaced between conjugated backbones. This corresponds well with the size of the spacing imaged via high resolution TEM. Additionally, a third spacing of 1.6 nm described by the (011) plane can be seen corresponding to the end capping hexyl stacking, which may be attributed to the second, more sensitive crystal population found in the some of the TEM images (Figure S4, Supporting Information).

2.2. Device Characteristics

Specific effects of the *p*-DTS(FBTTh$_2$)$_2$:PC$_{71}$BM morphology on charge generation and collection were probed by examining the photocurrent within the devices. The results of these studies are provided in **Figure 7**. By plotting the photocurrent against the effective voltage, differences in charge generation and collection between the as-cast, annealed, and optimized DIO conditions become evident. The effective voltage, that is the voltage at which no photocurrent is generated less the applied voltage, V_0–V, determines the strength of the electric field within the

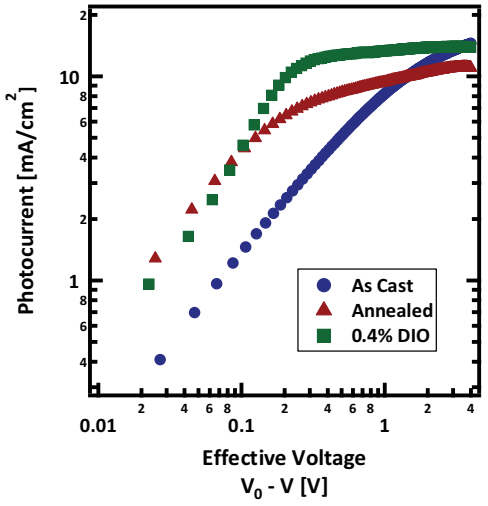

Figure 7. Photocurrent vs. effective voltage for three processing conditions as-cast (blue), thermally annealed at 130 °C (red), and with 0.4% DIO additive (green).

device and thus the driving force for charge extraction.[47] In the case of the 0.4% DIO and annealing conditions, the photocurrent quickly increases and then begins to plateau at relatively low effective voltages, ≈0.2 V; that is to say a very small driving force is needed for charge collection, suggesting good transport within the films and explaining the relatively high FF. In contrast, the photocurrent in as-cast devices does not begin to saturate, until an effective voltage of ≈4 V. The much stronger electric field required to sweep out photogenerated charges suggests relatively poor charge transport within these devices and is consistent with the absence of phase separated and ordered domains to provide effective percolation pathways.

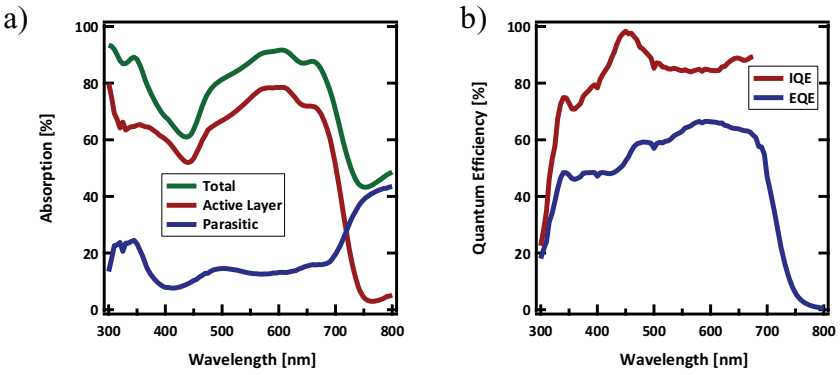

Figure 8. a) Total, parasitic, and active layer absorption of optimized device and b) internal quantum efficiency of optimized device.

At sufficiently high electric fields, we expect to collect nearly all of the generated charges within a device due to the strong driving force for extraction.[47] Thus, comparing the photocurrents at high effective voltages offers insight into the differences in photogeneration as a function of internal structure. In both the optimum DIO processed and as-cast film, the photocurrent at 4 V is ≈16 mA cm^{-2}, suggesting that photogeneration rates are quite similar, despite obvious differences in morphology. In the thermally annealed device, on the other hand, photocurrent saturates at ≈12 mA cm^{-2}. As these films are all of similar thickness, slight variations described in the film absorption cannot account for this substantial discrepancy in photocurrent. Rather, this is most likely evidence of a reduced photogeneration rate in the annealed film, which may be due to the larger domains seen via TEM; some generated excitons cannot diffuse to a D/A interface to produce free charges. These large domains may thus limit the short circuit current and maximum achievable PCE in annealed devices.

To further quantify how efficient the charge generation and extraction processes are in the optimum morphology, we have calculated the internal quantum efficiency (IQE) of the 0.4% DIO processed device. Following the technique developed by McGehee and colleages,[48] we determine the active layer absorption by subtracting the calculated parasitic absorption (due to PEDOT:PSS, Al, etc.) from the total device absorption, measured using a spectrometer fitted with an integrating sphere, as shown in **Figure 8**a.

Under the optimum conditions, we find that the IQE reaches nearly 100% for light at 445 nm and remains close to 90% efficient across the entire spectral range as seen in Figure 8b. Nearly all absorbed photons result in free charges, which are subsequently extracted, resulting in high short circuit current. Under ideal casting conditions, the device layer thickness was determined to be 100 ± 10 nm as measured by profilometry. While *p*-DTS(FBTTh$_2$)$_2$ has a relatively high optical density and covers a broad spectral range, solubility limitations prevent thicker film formation and thereby limit optical absorption of the active layer in devices. It can be seen in Figure 8a that the active layer never absorbs more than 80% of incident photons across the spectral range. This suggests that the J_{SC} in the optimum DIO processed devices is most limited by the absorption of the film rather than the charge generation or charge extraction processes.

3. Conclusions

Under the appropriate processing conditions, either by solvent additive or thermal annealing, the *p*-DTS(FBTTh$_2$)$_2$:PC$_{71}$BM system can achieve high efficiencies due to the ability to tune the nanoscale morphology. As-cast films show almost no crystallinity or phase separation, but rather a well-mixed blend of donor and acceptor. The result is the need for a large reverse bias applied to the devices to efficiently sweep out charges, leading to both a low FF and low J_{SC}, and thus a relatively low efficiency.

Thermal annealing leads to a drastic increase in performance; devices require a much lower effective voltage to sweep out the charges compared to the as-cast devices, leading to the increase in PCE to 5.8%. In the film, the thermal treatment leads to growth of wire-like domains of *p*-DTS(FBTTh$_2$)$_2$ with remarkable crystalline order as identified with high resolution TEM. The lattice spacings imaged by TEM correspond well with spacings in the crystal structure of *p*-DTS(FBTTh$_2$)$_2$ obtained with single crystal X-ray diffraction. The crystal structure shows that the molecule remains flat, and π-stacks with a relatively large overlapping area between adjacent molecules. We propose that the overlap of the conjugated backbones enables more efficient charge transport, explaining the increase in performance upon crystal growth. The saturated photocurrent in the annealed device is significantly lower than in the as-cast devices due to a reduction in charge generation, likely from a loss in interfacial area.

Addition of DIO to the blend solution also results in crystallization of p-DTS(FBTTh$_2$)$_2$ concomitant with an increase in PCE to 7.0%. Under ideal solvent additive conditions, the films show an inter-connected network of crystalline *p*-DTS(FBTTh$_2$)$_2$ domains with a characteristic size of 30 nm. The result is a high saturated photocurrent at very low effective voltages explaining both the high FF as well as extremely high internal quantum efficiency at short circuit, reaching over 90%. This demonstrates both efficient charge generation and collection.

4. Experimental Section

Transmission Electron Microscopy: Films were prepared for TEM in the same fashion as devices, atop PEDOT:PSS coated glass, however the PEDOT:PSS layer was not annealed and no cathode was deposited. The films were then scored and floated off of the substrate in deionized water and collected on a copper mesh grid coated with ultra-thin carbon coating (Electron Microscopy Sciences). Low resolution bright field images were taken on a FEI Tecnai G2 Sphera microscope operating at 200 kV. For good resolution, relatively long exposure times of 10–30 s were needed under low defocus conditions. High resolution images were taken on a FEI Titan FEG High Resolution microscope, using C-Flat Carbon holey carbon grids for stability. To achieve high resolution images, a low-dose imaging procedure was applied in which the sample was allowed to mechanically stabilize. A 1 µm defocus was applied to focus on the in-plane stacking within the film. The beam was then shifted electronically off of the optical axis to an undamaged area of the film for imaging. Using a 10 µm aperture, exposure times of 4 s were used to achieve images with average signals of 50–200 counts.

Cross-Section Fabrication: Samples for cross-section analysis were prepared atop a silicon substrate with a 200 nm oxide coating. The annealed bulk heterojunction was deposited as in devices atop PEDOT:PSS and annealed at 130 °C for 10 min in an inert atmosphere. A 30 nm TiOx layer was then deposited from an ethanol solution as described, and annealed at 70 °C for 10 min in air. Two successive layers of PEDOT:PSS were then deposited and annealed in air at 70 °C for 10 min each. The additive processed film was then cast and annealed at 70 °C as in devices. Again, a TiOx layer was deposited and annealed in air, two layers of PEDOT:PSS deposited, the final BHJ film cast, and 100 nm of aluminum deposited on top. A 20 µm × 1 µm × 5 µm deep slice was then milled out using an FEI Helios FIB microscope operating at 30 kV and 0.92 nA, undercut, and transferred to a copper support using an in-situ Omni probe system. The slice was then further thinned using a 30 kV ion beam operating at 93 pA. The final thinning was performed with a 5 kV ion beam at 0.16 nA to a final thickness of ≈75 nm.

Device Fabrication: Devices were prepared on cleaned, UV/ozone treated Corning 1737 glass patterned with 140 nm ITO. A PEDOT:PSS (Clevios P VP Al 4083) layer was first deposited and dried at 140 °C in ambient atmosphere. Active layers were spun at 1750 RPM to give 90–110 nm thicknesses (as determined using an Ambios XP-100 stylus profilometer) from solutions of *p*-DTS(FBTTh$_2$)$_2$ and PC$_{71}$BM at a weight ratio of 3:2 in chlorobenzene with or without 0.4% diiodooctane by volume, at an overall concentration of 35 mg mL^{-1}. Solutions were heated for several hours at 80 °C and residual solids filtered prior to casting at 80 °C. Films were allowed to dry for 30 min then heated to 70 °C for 10 min under inert atmosphere to drive off residual solvent. Cathodes were deposited by sequential thermal evaporation of 10 nm of calcium followed by 100 nm of aluminum. Three different electrode areas were tested (4.5 mm^2, 6 mm^2 and 15 mm^2), the largest illuminated through a 13.5 mm^2 aperture, to ensure current scaling. Device characteristics were measured under illumination by a simulated 100 mW cm^{-2} AM1.5G light source using a 300 W Xe arc lamp with an AM 1.5 global filter. Solar-simulator irradiance was calibrated using a standard silicon photovoltaic with a protective KG1 filter calibrated by the National Renewable Energy Laboratory.

IQE Measurements: External quantum efficiencies were determined using a 75W Xe source, monochromator, optical chopper, lock-in amplifier, and a National Institute of Standards and Technology calibrated silicon photodiode was used for power-density calibration. Equivalent films were also fabricated in which the entire top surface was covered with Ca/Al, rather than a patterned electrode. These films were then used to determine the absolute total reflectivity using a Perkin Elmer Lambda 750 UV/Visible light spectrometer fitted with a 60 mm integration sphere. Thickness measurements were obtained with an Ambios XP 100 profilometer and optical constants were taken from the absorption spectra. Parasitic absorption was modeled using a transfer matrix model MATLAB program available online at http://mcgeheegroup.stanford.edu/transfermatrix.

Supporting Information

Supporting Information is available from the Wiley Online Library or from the author.

Acknowledgements

The authors are grateful for financial support from the Center for Energy Efficient Materials, an Energy Frontier Research Center funded by the Office of Basic Energy Sciences of the US Department of Energy (DE-DC0001009, for device optimization, cross sectional TEM analysis and synthesis of *p*-DTS(FBTTh$_2$)$_2$), the National Science Foundation American Competitiveness and Innovation Award (DMR-1035480, for single crystal studies) the National Science Foundation Graduate Research Fellowship (DGE-1144085, for device characterization and X-ray analysis), and the National Science Foundation (DMR-0856060 for low-dose high-resolution TEM analysis). This work made use of MRL Central Facilities supported by the MRSEC Program of the National Science Foundation under award No. DMR05-20415.

Received: January 9, 2013
Revised: March 13, 2013
Published online: May 22, 2013

[1] B. Kippelen, J.-L. Brédas, *Energy Environ. Sci.* **2009**, *2*, 251.
[2] J. Peet, A. J. Heeger, G. C. Bazan, *Acc. Chem. Res.* **2009**, *42*, 1700.
[3] F. C. Krebs, *Sol. Energy Mater. Sol. Cells.* **2009**, *93*, 465.
[4] X. Yang, J. Loos, *Macromolecules* **2007**, *40*, 1353.
[5] J. Rivnay, R. Steyrleuthner, L. H. Jimison, A. Casadei, Z. Chen, M. F. Toney, A. Facchetti, D. Neher, A. Salleo, *Macromolecules* **2011**, *44*, 5246.
[6] O. V. Mikhnenko, H. Azimi, M. Scharber, M. Morana, P. W. M. Blom, M. A. Loi, *Energy Environ. Sci.* **2012**, *5*, 6960.
[7] D. T. Duong, B. Walker, J. Lin, C. Kim, J. Love, B. Purushothaman, J. E. Anthony, T.-Q. Nguyen, *J. Polym. Sci., Part B: Polym. Phys.* **2012**, *50*, 1405.
[8] B. C. Thompson, J. M. J. Fréchet, *Angew. Chem., Int. Ed.* **2008**, *47*, 58.
[9] B. Walker, C. Kim, T.-Q. Nguyen, *Chem. Mater.* **2011**, *23*, 470.
[10] A. Mishra, P. Bäuerle, *Angew. Chem., Int. Ed.* **2012**, *51*, 2020.
[11] J. Zhou, X. Wan, Y. Liu, Y. Zuo, Z. Li, G. He, G. Long, W. Ni, C. Li, X. Su, Y. Chen, *J. Am. Chem. Soc.* **2012**, *134*, 16345.
[12] Y. Sun, G. C. Welch, W. L. Leong, C. J. Takacs, G. C. Bazan, A. J. Heeger, *Nat. Mater.* **2012**, *11*, 44.
[13] T. S. van der Poll, J. A. Love, T.-Q. Nguyen, G. C. Bazan, *Adv. Mater.* **2012**, *24*, 3646.
[14] M. Chen, W. Fu, M. Shi, X. Hu, J. Pan, J. Ling, H. Li, H. Chen, *J. Mater. Chem.* **2013**, *1*, 105.
[15] L.-C. Chi, H.-F. Chen, W.-Y. Hung, Y.-H. Hsu, P.-C. Feng, S.-H. Chou, Y.-H. Liu, K.-T. Wong, *Sol. Energy Mater. Sol. Cells.* **2013**, *109*, 33.
[16] G. He, Z. Li, X. Wan, J. Zhou, G. Long, S. Zhang, M. Zhang, Y. Chen, *J. Mater. Chem. A.* **2013**, *1*, 1801.
[17] W. L. Leong, G. C. Welch, J. Seifter, J. H. Seo, G. C. Bazan, A J. Heeger, *Adv. Energy Mater.* **2012**, *3*, 356.
[18] S. Ma, Y. Fu, D. Ni, J. Mao, Z. Xie, G. Tu, *Chem. Commun.* **2012**, *48*, 11847.
[19] M. J. Banach, R. H. Friend, H. Sirringhaus, *Macromolecules* **2003**, *36*, 2838.
[20] W. L. Leong, G. C. Welch, L. G. Kaake, C. J. Takacs, Y. Sun, G. C. Bazan, A. J. Heeger, *Chem. Sci.* **2012**, *3*, 2103.
[21] A. Garcia, G. C. Welch, E. L. Ratcliff, D. S. Ginley, G. C. Bazan, D. C. Olson, *Adv. Mater.* **2012**, *24*, 5368.

[22] S. C. Price, A. C. Stuart, L. Yang, H. Zhou, W. You, *J. Am. Chem. Soc.* **2011**, *133*, 4625.
[23] J. Peet, J. Y. Kim, N. E. Coates, W. L. Ma, D. Moses, A. J. Heeger, G. C. Bazan, *Nat. Mater.* **2007**, *6*, 497.
[24] J. Mizuguchi, *J. Phys. Chem.* **2000**, *104*, 1817.
[25] T. Erb, U. Zhokhavets, G. Gobsch, S. Raleva, B. Stühn, P. Schilinsky, C. Waldauf, C. J. Brabec, *Adv. Funct. Mater.* **2005**, *15*, 1193.
[26] B. Walker, A. B. Tamayo, X.-D. Dang, P. Zalar, J. H. Seo, A. Garcia, M. Tantiwiwat, T.-Q. Nguyen, *Adv. Funct. Mater.* **2009**, *19*, 3063.
[27] C. B. Carter, D. Williams, in *Transmission Electron Microscopy: A Textbook for Materials Science,* 2nd Ed., Springer, New York **2009**, Ch. 4, 22, 23,28.
[28] T. Martens, J. D'Haen, T. Munters, Z. Beelen, L. Goris, J. Manca, M. D'Olieslaeger, D. Vanderzande, L. De Schepper, R. Andriessen, *Synth. Met.* **2003**, *138*, 243.
[29] D. M. De Longchamp, R. J. Kline, A. Herzing, *Energy Environ. Sci.* **2012**, *5*, 5980.
[30] A. J. Lovinger, H. E. Katz, A. Dodabalapur, *Chem. Mater.* **1998**, *10*, 3275.
[31] C. Kübel, L. González-Ronda, L. F. Drummy, D. C. Martin, *J. Phys. Org. Chem.* **2000**, *13*, 816.
[32] D. C. Martin, J. Chen, J. Yang, L. F. Drummy, C. Kübel, *J. Polym. Sci. Part B: Polym. Phys.* **2005**, *43*, 1749.
[33] J. Loos, J. K. J. Van Duren, F. Morrissey, R. A. J. Janssen, *Polymer.* **2002**, *43*, 7493.
[34] K. R. Graham, P. M. Wieruzewski, R. Stalder, M. J. Hartel, J. Mei, F. So, J. R. Reynolds, *Adv. Funct. Mater.* **2012**, *22*, 4801.
[35] J. S. Moon, C. J. Takacs, Y. Sun, A. J. Heeger, *Nano Lett.* **2011**, *11*, 1036.
[36] J. Y. Kim, K. Lee, N. E. Coates, D. Moses, T.-Q. Nguyen, M. Dante, A. J. Heeger, *Science.* **2007**, *317*, 222.
[37] J. S. Moon, C. J. Takacs, S. Cho, R. C. Coffin, H. Kim, G. C. Bazan, A. J. Heeger, *Nano Lett.* **2010**, *10*, 4005.
[38] N. I. Kato, *J. Electron. Microsc.* **2004**, *53*, 451.
[39] J. E. Anthony, *Chem. Rev.* **2006**, *106*, 5028.
[40] J. E. Anthony, J. S. Brooks, D. L. Eaton, S. R. Parkin, *J. Am. Chem. Soc.* **2001**, *123*, 9482.
[41] S. Haid, A. Mishra, M. Weil, C. Uhrich, M. Pfeiffer, P. Bäuerle, *Adv. Funct. Mater.* **2012**, *22*, 4322.
[42] S. Hotta, K. Waragai, *Adv. Mater.* **1993**, *5*, 896.
[43] M.-H. Yoon, A. Facchetti, C. E. Stern, T. J. Marks, *J. Am. Chem. Soc.* **2006**, *128*, 5792.
[44] C. Kim, J. Liu, J. Lin, A. B. Tamayo, B. Walker, G. Wu, T.-Q. Nguyen, *Chem. Mater.* **2012**, *24*, 1699.
[45] J. Liu, B. Walker, A. Tamayo, Y. Zhang, T.-Q. Nguyen, *Adv. Funct. Mater.* **2012**, *23*, 47.
[46] V. Coropceanu, J. Cornil, D. A. da Silva Filho, Y. Olivier, R. Silbey, J.-L. Brédas, *Chem. Rev.* **2011**, *107*, 926.
[47] V. D. Mihailetchi, L. J. A. Koster, J. C. Hummelen, P. W. M. Blom, *Phys. Rev. Lett.* **2004**, *93*, 216601.
[48] G. F. Burkhard, E. T. Hoke, M. D. Mc Gehee, *Adv. Mater.* **2010**, *22*, 3293.